Supporting information for: Plasmonic Band Structure Controls Single Molecule Fluorescence

Lutz Langguth,*,† Deep Punj,‡ Jérôme Wenger,‡ and A. Femius Koenderink†

Center for Nanophotonics, FOM Institute for Atomic and Molecular Physics (AMOLF), Science Park 104, 1098 XG Amsterdam, The Netherlands, and CNRS, Aix-Marseille Université, Ecole Centrale Marseille, Institut Fresnel, Campus de St Jérôme, 13397 Marseille, France

E-mail: l.langguth@amolf.nl

In this supplement we describe

1. Measurement protocol and FCS data
2. Square lattice theoretical analysis
3. Finite Element Simulations

Measurement protocol, including FCS calibration

In our measurement protocol (set up diagram, see Figure S1), we first perform confocal imaging and FCS. For each structure we first scan the sample in the xy-plane to acquire a confocal image

*To whom correspondence should be addressed

†Center for Nanophotonics, FOM Institute for Atomic and Molecular Physics (AMOLF), Science Park 104, 1098 XG Amsterdam, The Netherlands

‡CNRS, Aix-Marseille Université, Ecole Centrale Marseille, Institut Fresnel, Campus de St Jérôme, 13397 Marseille, France

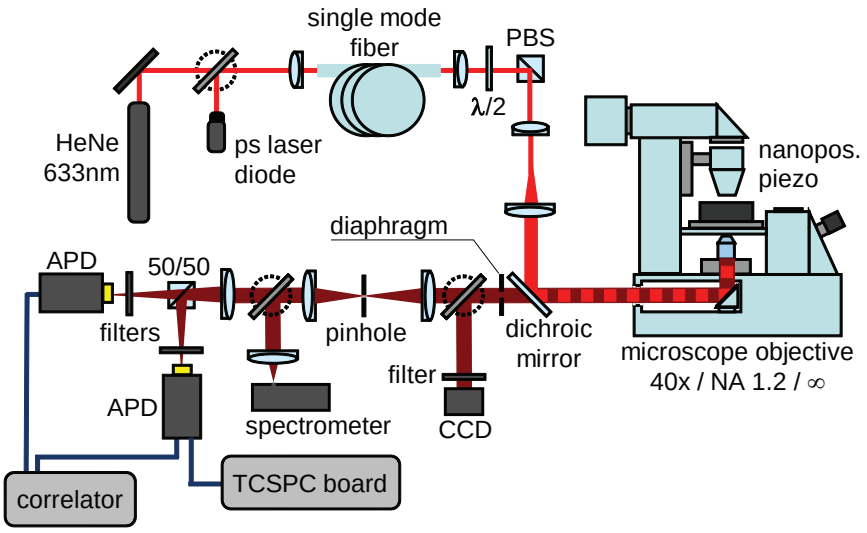

Figure S1: Diagram of the setup consisting of an inverted microscope, a CCD for Fourier imaging, and a set of APDs coupled to timing electronics as detectors confocal with the diffraction limited pump spot.

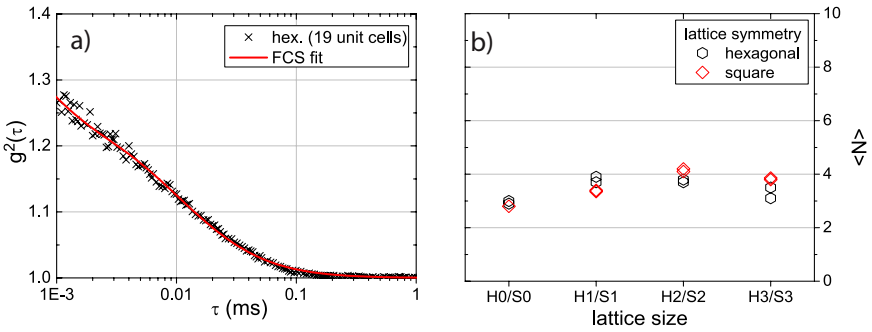

Figure S2: (a) Typical fluorescence correlation spectroscopy (FCS) trace. This trace is obtained from the central aperture in a hexagonal lattice of radius that is twice the pitch (two shells around the central hole). The data is excellently fitted according to the procedure in Ref.[S1,S2] We use the very same analysis method to extract the number $\langle N \rangle$ of molecules probed, plotted as a function of structure size in panel (b), for the square and hexagonal lattices (square resp. hexagonal plot symbols).

(excitation power: $200\ \mu$W) of the fluorescence intensity using the APD photodetectors. We clearly resolve the individual holes which are separated by 440 nm at count rates above 300 kHz when exciting the center of an aperture. The low count rate of < 1 kHz in the black areas of the scan shows that 150 nm thick gold effectively shields the fluorophores that are not close to a hole from being excited or coupling out. For all subsequent measurements of a structure we positioned the sample such, that only the center hole is excited.

We characterize the center aperture of each structure by conducting a FCS measurement (excitation power: $40\ \mu$W) which yields the mean number $\langle N \rangle$ of molecules contributing to fluorescence in the aperture, and their diffusion time. An FCS measurement for the two-row hexagonal structure is shown in Figure S2 with the corresponding fit to standard diffusion theory.[S1,S2] The diffusion time confirms that the fluorescence emission originates from molecules performing normal diffusion without sticking to any interface. In Figure S2d (bottom) we plot the average number of molecules $\langle N \rangle$ for all measured structures and compare to reference measurements which we have taken in an open solution. Importantly we find that the average number of fluorophores measured for all nano-apertures falls in the range of $\langle N \rangle = 3.5 \pm 0.7$ and hardly depends on the structure surrounding the pumped hole. The small variation of at most 20% in $\langle N \rangle$ measured by FCS indicates equal geometric size of the apertures.

Subsequent to calibration of the mean number of molecules probed, we perform a lifetime measurement as described in the main text. Then we switch to back aperture imaging. We position a mirror behind the dichroic beam splitter to direct the radiation to a CCD array, while still only pumping the center-aperture with the He-Ne laser (now $P = 200\ \mu$W; exposure time $T = 25$ s). We collect all the emitted radiation and there is no spatial filtering by a pinhole as in the calibration measurements that employ the APD detectors.

In the analysis of the fourier images, we reconstruct the polar plot of radiated flux per solid angle. We average the radiated power over the azimuthal angle φ from 0 to 2π. The such obtained polar plot ranging from $\theta = 0..\pi/2$ is mirrored around $\theta = 0$ and plotted for $\theta = -\pi/2..\pi/2$ for a better visual appearance.

Square lattices

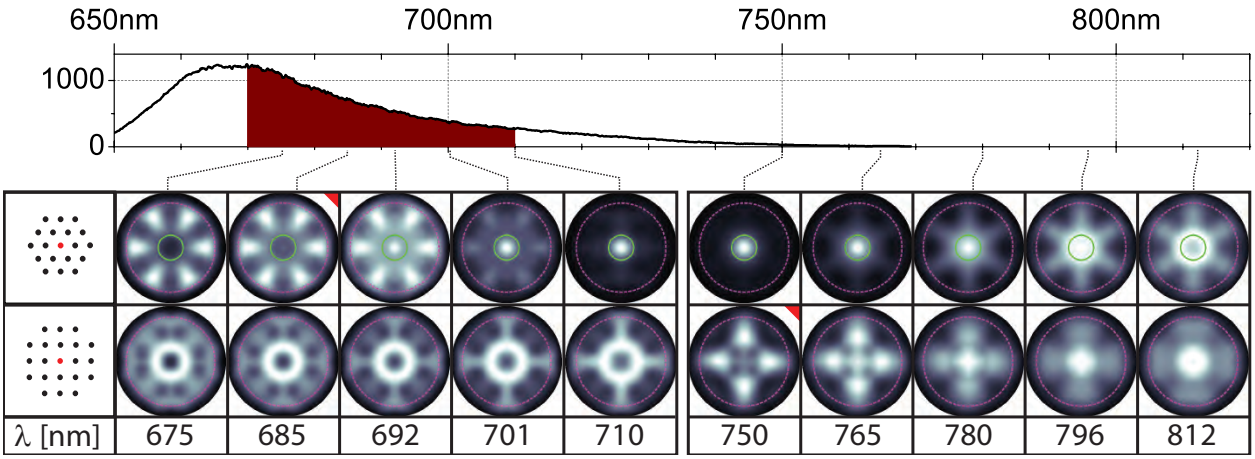

Figure S3: top) Fluorescence emission spectrum of a single nano-aperture infiltrated with Alexa647. The part of the spectrum filled in dark red denotes the spectrum transmitted by the bandpass filter in front of the CCD. bottom) simulated radiation patterns for different wavelength for the hexagonal and square S2 lattice. Radiation patterns marked with a red triangle indicate the wavelength where the beaming into forward direction has just stopped. To allow comparison to the experimental data, the magenta dashed line denotes the maximum collection angle of the experiment.

As reported as Fig. 3 of the main manuscript, to further confirm the defining role of the band structure for the radiation pattern, we performed measurement on square lattices of different sizes, all with the same pitch of $a = 440$ nm as the hexagonal structures, and with the same hole size of 140 nm. Here we provide the full wave analysis for the corresponding structure. COMSOL simulations (see below for details) of the square lattice shown in Figure S3 alongside the results for hexagonal lattices confirm that the square lattice is similar in physics, but redshifted in features, compared to the hexagonal case. For both lattices a transition occurs from beaming into the forward direction for long wavelengths, to emission into sidelobes for shorter wavelength. While for the hexagonal lattice the forward emission vanishes around 690 nm, for the square lattice the transition happens already around 750 nm owing to the factor $\sqrt{3/4}$ difference in reciprocal lattice size. We notice that the simulated radiation pattern does not change significantly in the spectral region of the experiment ($670-710$ nm). The simulation is consistent with the observed dip into the forward direction and the fact that most of the intensity is radiated into a ring at an angle of approximately

20° relative to the sample normal. In the folded dispersion relations we see the $\Gamma-$ point of the square lattice is redshifted ≈ 50 nm compared to the hexagonal lattice (see Figure S4).

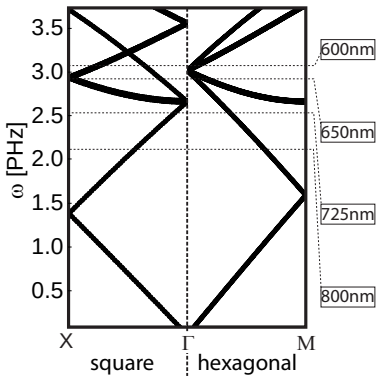

Figure S4: Crosscut along a reciprocal lattice vectors through the folded dispersion relation of a SPP on a Gold-glass interface for the square lattice (left) and the hexagonal lattice (right), both with 440 nm pitch

COMSOL simulations

Figure S5 shows the layout of the simulation domain, which is a cylinder with axis normal to the sample substrate that is a stack of water and the perforated gold film, on top of which we place a hemispherical dome of glass. The dielectric constants are reported in the main manuscript. The simulation domain is closed on all sides with perfectly matched layers ($\sim \lambda/2$ thickness), except at the symmetry planes $x = 0$, $y = 0$ where perfect electric/magnetic conductor boundary conditions allow to reduce the computational load. To ensure accurate results we use a fine discretization < 10 nm of the metal surfaces, further refining the mesh near the interface into the metal, glass and water using boundary layer meshing.

The near-to-far-field transformation requires choosing a surface on which to record the near-field. Since the Stratton-Chu integral is rigorously valid only for closed surfaces and in absence of stratification, the obtained far field should be viewed as a finite-truncation radius approximation to the angular spectrum representation integral that rigorously describes radiation patterns near surfaces. By choosing as surface for the near to far field transformation a large dome concentric with the spherical wave seen to originate from the structure and by truncating the dome 300 nm above

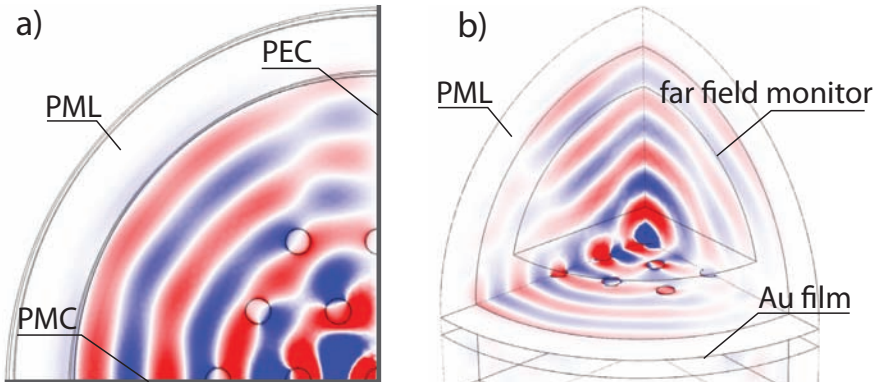

Figure S5: Layout of the COMSOL 4.3 finite element simulation. (a) Top view onto the sample plane, highlighting the periodic boundary conditions and absorbing boundary conditions used for an x-oriented dipole (color code shows a snapshot of the z-component of the electric field). We use the symmetry of the problem to reduce the size of the computation box. The symmetry plane normal to the dipole orientation is implemented as a perfect electric conductor (PEC), the symmetry plane parallel to the source is set as a perfect magnetic conductor (PMC). The entire computation domain is closed by perfectly matched layers (PML). The color indicates of z-component of the electric field amplitude at the gold-glass interface. b) Tilted view on the computation domain including the surface used to do the near to far-field transformation. The color coding here represents the amplitude of the x-component of the electric field.

the sample surface, we find reasonably accurate far fields. A key aspect of this choice is that truncation of the dome above the surface removes unphysical contributions of the unscattered guided plasmon that appear if the surface is chosen closer to the gold film. Indeed, the dome ends above the evanescent tail of the guided plasmon so that it collects plasmon fields scattered out by the holes into the radiative continuum, but avoids contributions of the unscattered guided plasmon. On basis of benchmark comparisons of this approach to theory for dipole sources above unpatterned interfaces,[S3,S4] we estimate accuracy to within $10-20$ %. We have furthermore established that the radiation patterns barely change if we increase the simulation box size, including the near-to-far field transformation dome by a factor 3 in radius (while keeping the same truncation height).

References

(S1) Wenger, J.; Gérard, D.; Dintinger, O., J.and Mahboub; Bonod, N.; Popov, E.; Ebbesen, T. W.; Rigneault, H. Emission and Excitation Contributions to Enhanced Single Molecule Fluorescence by Gold Nanometric Apertures. *Opt. Expr.* **2008**, *16*, 3008.

(S2) Aouani, H.; Mahboub, O.; Bonod, N.; Devaux, E.; Popov, E.; Rigneault, H.; Ebbesen, T. W.; Wenger, J. Bright Unidirectional Fluorescence Emission of Molecules in a Nanoaperture with Plasmonic Corrugations. *Nano Lett.* **2011**, *11*, 637–644.

(S3) Lukosz, W.; Kunz, R. E. Light Emission by Magnetic and Electric Dipoles Close to a Plane Interface. I. Total Radiated Power. *J. Opt. Soc. Am.* **1977**, *67*, 1607–1615.

(S4) Lukosz, W.; Kunz, R. E. Light Emission by Magnetic and Electric Dipoles Close To A Plane Dielectric Interface. II. Radiation Patterns of Perpendicular Oriented Dipoles. *J. Opt. Soc. Am.* **1977**, *67*, 1615–1619.